UNIVERSITÄT
DUISBURG
ESSEN

Offen im Denken

Universität Duisburg-Essen
Institut für Mechanik
Fakultät für Ingenieurwissenschaften
Abteilung Bauwissenschaften
Prof. Dr.-Ing. J. Schröder

An engineering tool to estimate eigenstresses in three-dimensional patient-specific arteries

by Jörg Schröder & Markus von Hoegen

Report - Preprint	No. 115

30. September 2015

Editor: Prof. Dr.-Ing. habil. Jörg Schröder

submitted to
Computer Methods in Applied Mechanics and Engineering

Universitätsstraße 15, 45141 Essen, Germany

An engineering tool to estimate eigenstresses in three-dimensional patient-specific arteries

Jörg Schröder[†] & Markus von Hoegen[‡]

Institute of Mechanics, Faculty of Engineering Science / Dept. Civil Engineering
University of Duisburg-Essen, 45141 Essen, Universitätsstr. 15, Germany
[†]e-mail: j.schroeder@uni-due.de, phone: +49 201 183 2708, fax: +49 201 183 2680
[‡]e-mail: markus.von-hoegen@uni-due.de, phone: +49 201 183 3091, fax: +49 201 183 2680

Abstract

In this contribution we propose an engineering based approach to incorporate eigenstress distributions in arteries. Eigenstresses are known for a variety of biological tissues. In the case of arterial walls the so called opening angle experiment is frequently used to characterize the residual strains/stresses. Assuming that the transmural stress distribution of suitable stress measures should be smooth, a residual stress tensor is directly estimated from the Cauchy stresses. These stress measures are constructed in such a way that the basic biophysiological characteristics, like the fiber orientations which are taken into account by suitable structural tensors, are adequately respected. In order to achieve reasonable eigenstress distributions in the arteries the local stress measures should approach spatial-sector averaged values. These ideas are imbedded in an algorithm to update the residual stress tensor incrementally. An ideal tube and degenerated patient-specific arteries from medical imaging are used to demonstrate the performance of the proposed procedure and to estimate the opening angle.

Keywords: Biomechanics, Residual Stress, Vascular Wall

1 Introduction

Medical imaging allows one to reconstruct patient-specific geometries of arteries. In the future numerical simulations could help to better understand mechanically influenced processes in blood vessels, to improve medical treatment and to asses the risk potential of degenerated sections. Credible assessments require advanced models, considering multiple biological phenomena. One of these are the residual stresses arising in a number of biological soft tissues, in particular in arterial walls. A reliable and precise description of the transmural stresses might be beneficial to decide on the most appropriate medical treatment of vascular diseases in the future and the wall stress might be established as a diagnostic indicator. For example plaque rupture is supposed to be initiated by stress concentrations and the application of suitable stress criteria to gauge the risk could be desirable, see Cheng et al. [1993] or Li et al. [2006]. Possible effects of residual stresses on plaque rupture were studied numerically in Ohayon et al. [2007]. The authors concluded that the stresses in the fibrous cap are overestimated when residual stresses are neglected. Auricchio et al. [2013] investigated, disregarding eigenstresses, the influence of constitutive material laws on vessel straightening and lumen gain induced by carotid artery stenting. They formulate the challenging and forward-looking task to combine medical imaging and finite element analysis to become a "procedure planning tool supporting the clinical practice". Furthermore, the understanding of residual stresses might contribute to a better understanding in possibly stress driven growth and remodeling processes, cf. Greenwald et al. [1997].

An arterial segment which is free from any external load and is radially sliced will deform into a horseshoe-shaped configuration and the so called opening angle can be measured in order to classify the stress release. In light of the fact, that the opening angle is larger for the inner rings of the same cross-section, Greenwald et al. [1997] concluded that a single cut is not sufficient to release the complete residual strains. Moreover they stated that the higher elastin content in the inner layers is responsible for that. The fact that the opening angle becomes larger with age, gives cause to suspect that incompatible growth is a dominant factor for the emergence of eigenstresses. The incompatibility of the strains induced by biological growth enforces residual stresses. The formation of growth induced stresses was studied theoretically in Rodriguez et al. [1994], Skalak et al. [1996] and Araujo and McElwain [2005]. To tackle the origin of eigenstresses is not in the scope of this paper. Additional studies regarding that topic are provided in Zeller and Skalak [1998], Lanir [2009] or Cardamone et al. [2009]. The latter publication is part of a series of papers dealing with the influence of the individual tissue constituents on the mechanical behavior, imbedded in the framework of mixture theory. This model is strongly motivated by the biological evolution of arteries and it is able to relate the single constituents to individual stress free configurations.

One major difficulty when estimating the residual stresses from the opening angle concerning the transferability to in-vivo conditions is that excised in-vitro configurations are self-equilibrating. That means the exact in-vivo state can not be estimated since the residual stresses which are released are altered compared to the in-vivo configuration. To reduce the appearance of residual strains to a plane strain problem which is only described by one parameter, the opening angle, is not sufficient. In Holzapfel and Ogden [2010] it was reported that the axial pre-stretch is an important factor which has a strong effect and should not be neglected in numerical calculations. In Holzapfel et al. [2005] a mean in-vivo pre-stretch of 1.044 of a human coronary artery is reported. The stretch is defined as the quotient of the in-vivo segment length and the excised segment length.

Sense of proportion should also be taken with regard to the comparability of laboratory results: Position along the vascular tree, species, age, sex and diseases of the samples as well as the testing conditions considerably affect the results.

Huang and Yen [1998] found that the opening angle tends to increase with an increasing general size of the artery. Further, the artery was found to continue to open up to 20 minutes after the excised segment is radially cut which is in accordance with several studies, see for example Han and Fung [1991]. Hence, residual stresses could also have a viscoelastic characteristic. Azeloglu et al. [2008] investigated experimentally and numerically how inhomogeneous proteoglycan distributions over the vessel wall may influence the opening angle. It was shown that the opening angle increases with increasing osmotic swelling pressure, caused by lower salt concentrations of the bathing environment.

The opening angle is subject to large fluctuations along the vascular tree, see Fung and Liu [1989]. The widely-held assumption that the residual stresses are compressive on the inner layers and tensile on the outer layers is supported by the observation, that the elastic lamina tends to buckle in the unloaded state, cf. Fung and Liu [1992]. Further, Han and Fung [1991] used markers to determine local strains in porcine and canine trachea. They found that the residual strains vary significantly with respect to the circumferential position in curved, but not in straight arteries.

Badel et al. [2012] investigated small cube shaped arterial samples excised from segments

which were fixed with needles. After removing the needles the residual strain field was determined based on optical full-field measurement. The obtained data was then used to deduce the residual stress field. The major advantage of that novel methodology compared to the classical opening angle measurement is that only a local part is tested and therefore the inhomogeneity of the residual stresses, also over the cross-section, may be accounted for.

The parameter fitting to tension and compression tests of excised arterial stripes neglects the described effects, since the residual stresses/strains are already released. Blood vessels under physiological blood pressure exhibit eigenstresses in a range that contributes to a smooth stress distribution with moderate stress gradients across the vessel wall. It should be noted that also the active response and osmotic swelling are believed to contribute to that effect. Besides, it is possible to obtain material parameters from in-vitro inflation tests which reflect the real in-vivo motion according to the blood pressure. In this case only the axial pre-stretch is released which can be considered in the experimental setup during the inflation, cf. for example Blondel et al. [2001] and Kim and Baek [2011]. Moreover, Genovese [2009] developed full-field measurements for inflation tests. From the full-field experimental data Avril et al. [2010] derived material parameters by making use of an inverse-method which is called virtual fields method.

A series of publications deals with the incorporation of initial, possibly incompatible, strain fields, deduced from the opening angle, in numerical simulations. In Holzapfel et al. [2000], Holzapfel and Gasser [2007], Peña et al. [2006], Alastrué et al. [2007] and Bustamante and Holzapfel [2010] models with varying complexity are implemented requiring the (layer-specific) opening angle and axial pre-stretch as input parameters in order to construct an initial deformation gradient. In contrast, in Balzani et al. [2007] a displacement driven scheme was applied to close the gap between a stress-free opened configuration and the closed, unloaded configuration. Shams et al. [2011] proposed a general setup to formulate strain energy functions which depend on invariants that couple finite deformations and an initial stress tensor. Wang et al. [2014] adapted that scheme to simulate residual stresses in the left ventricle and deduced residual stress tensors from the opening angle and residual strain full-field measurements. The uniformity hypothesis for the in-vivo circumferential strain or stress across the radius, originally formulated in Takamizawa and Hayashi [1987], was assessed in Chen and Eberth [2012] by formulating an optimization problem for the constitutive function. Based on the same hypothesis Polzer et al. [2013] formulated a growth model where the growth parameter is estimated from the current stress state. The growth criterion is designed such that the stress distribution becomes more homogenous.

A novel scheme for the computation of eigenstresses in arteries was proposed by Schröder and Brinkhues [2014] and implemented for two-dimensional boundary value problems. Based on the above mentioned hypothesis in Takamizawa and Hayashi [1987] they defined local averaged stress invariants with respect to subdomains of the cross-section of the artery which are used for the modification of the actual stress state. The approach is clearly of a descriptive or phenomenological nature. Usually the stresses are assumed to be the dominant trigger in the evolution of arterial growth and in Taber and Humphrey [2001] it has been stated that it is rather preferable to use stress driven growth models instead of strain driven models in order to obtain reasonable opening angles in simulations. In this study we will also focus particularly on the stresses and make use of the

geometrical constraints concerning the stresses in order to estimate suitable residual stress distributions. Throughout this study the active response of the smooth muscle cells which contributes to the decrease of the in-vivo stress/strain gradient is neglected. The additional decrease of the gradient because of the smooth muscle cell activation has recently been modeled in Zheng and Ren [2016].

In this contribution the method proposed in Schröder and Brinkhues [2014] is extended. The underlying strain measures, which are used to estimate the residual stresses directly from the current stress state, are improved in view of the biological characteristics and the numerical robustness. Furthermore, the approach is extended to three-dimensional simulations. The method is applied to three-dimensional patient-specific arteries, which were reconstructed from medical imaging.

2 Constitutive modeling of soft biological tissues

A body $\mathcal{B} \subset \mathbb{R}^3$ in the undeformed reference state is parametrized in $\boldsymbol{X}$, while the same body $\mathcal{S}$ in the deformed state is parametrized in $\boldsymbol{x}$. Both configurations are connected by the motion $\boldsymbol{\varphi}$ which maps points $\boldsymbol{X} \in \mathcal{B}$ onto $\boldsymbol{x} \in \mathcal{S}$, i.e. $\boldsymbol{x} = \boldsymbol{\varphi}(\boldsymbol{X})$. The deformation gradient is defined by $\boldsymbol{F} = \nabla\boldsymbol{\varphi}(\boldsymbol{X})$ with $\det\boldsymbol{F} = J > 0$ and the right Cauchy-Green tensor by $\boldsymbol{C} = \boldsymbol{F}^T\boldsymbol{F}$. An often used assumption is that arterial walls exhibit quasi-incompressible material behavior. Hence, a mixed finite element formulation is required in order to avoid volume locking effects. We consider the two-field functional

$$\Pi(\boldsymbol{\varphi}, \theta) = \int_{\mathcal{B}} \psi\left(\overline{\boldsymbol{C}}\right)\, \mathrm{d}V + \Pi_{\text{ext}}(\boldsymbol{\varphi}) \quad \text{with} \quad \Pi_{\text{ext}}(\boldsymbol{\varphi}) = -\int_{\mathcal{B}} \boldsymbol{x}\cdot\boldsymbol{b}\, \mathrm{d}V - \int_{\partial\mathcal{B}_\sigma} \boldsymbol{x}\cdot\boldsymbol{t}\, \mathrm{d}A\ , \quad (1)$$

where the modified right Cauchy-Green tensor is given by $\overline{\boldsymbol{C}} = \left(\frac{\theta}{J}\right)^{2/3}\boldsymbol{C}$. Here, $\theta = v_e/V_e$ denotes the element wise constant ratio of the element volume V_e in the reference and the element volume $v_e = \int_{\mathcal{B}_e} J\, \mathrm{d}V_e$ in the actual configuration and is called volume dilation, cf. Nagtegaal et al. [1974]. The free energy ψ is a function of $\overline{\boldsymbol{C}}$ and will be mathematically defined later. The second part $\Pi_{\text{ext}}(\boldsymbol{\varphi})$ covers the external forces, where $\boldsymbol{b}$ denotes the body forces and $\boldsymbol{t}$ the surface tractions, acting on $\partial\mathcal{B}_\sigma$. The boundary $\partial\mathcal{B}$ is decomposed into the "Dirichlet" and "Neumann" part $\partial\mathcal{B}_u$ and $\partial\mathcal{B}_\sigma$, respectively, satisfying $\partial\mathcal{B} = \partial\mathcal{B}_u \bigcup \partial\mathcal{B}_\sigma$ and $\partial\mathcal{B}_u \bigcap \partial\mathcal{B}_\sigma = \varnothing$. In order to solve the constrained minimization problem we apply an augmented solution scheme to enforce the quasi-incompressibility condition. Thus, we consider the functional

$$\mathcal{L}(\boldsymbol{\varphi}, \theta, \lambda) = \Pi(\boldsymbol{\varphi}, \theta) + \int_{\mathcal{B}} \lambda(\theta - 1)\, \mathrm{d}V\ . \quad (2)$$

In the context of constraint optimization and the augmented Lagrangian solution strategy to prevent ill-conditioning of the stiffness matrix we refer to Hestenes [1969], Powell [1969], Glowinski and Le Tallec [1984], Glowinski and Le Tallec [1988] and Glowinski and Le Tallec [1989]. The Lagrange multiplier λ will enforce θ to be close to the incompressibility constraint $J = 1$ with a permitted discrepancy of $\pm 1\%$. For the update of the Lagrange multiplier a simultaneous Uzawa algorithm according to Simo and Taylor [1991] with

$$\lambda_{n+1} = \lambda_n + \kappa\,(\theta_n - 1) \quad (3)$$

is chosen. Here, κ is a penalty like parameter. In a simultaneous Uzawa algorithm the multiplier is updated after every Newton-iteration step. For that reason the algorithm does not provide quadratic convergence, but therefore dramatically decreases the computational cost in the present application field compared to a nested Uzawa algorithm, where the multiplier is updated after convergence and the iteration is repeated until the discrepancy is satisfied in each element. The performance of the augmented Lagrange approach in the context of arterial walls was studied in Brinkhues et al. [2013]. Throughout this work we use polyconvex energy functions which guarantee in combination with the coercivity condition the existence of minimizers, see Ball [1977]. Furthermore, polyconvex functions satisfy the Legendre-Hadamard condition and therefore ensure real wave speeds. The free energy

$$\psi = \psi(I_1, I_2, I_3, J_4^{(a)}, J_5^{(a)}) \tag{4}$$

is formulated in terms of invariants, where $I_1 = \operatorname{tr} \overline{\boldsymbol{C}}$, $I_2 = \operatorname{tr}[\operatorname{cof} \overline{\boldsymbol{C}}] = \operatorname{tr}\left[\det(\overline{\boldsymbol{C}})\overline{\boldsymbol{C}}^{-1}\right]$ and $I_3 = \det \overline{\boldsymbol{C}}$. Collagen fibers have a major impact on arterial wall mechanics. These crosswise orientated fibers, see also Fig. 1, provide a lot more stiffness in the high strain regime than the surrounding matrix material. Therefore, we consider the structural tensors

$$\boldsymbol{M}_{(a)} = \boldsymbol{A}_{(a)} \otimes \boldsymbol{A}_{(a)} \qquad \text{with} \qquad \operatorname{tr} \boldsymbol{M}_{(a)} = 1 \quad \text{and} \quad \|\boldsymbol{A}_{(a)}\| = 1 \,, \tag{5}$$

where $\boldsymbol{A}_{(a)}$ for $a = 1, 2$ are unit vectors in the reference configuration. The mixed invariants of $\overline{\boldsymbol{C}}$ and $\boldsymbol{M}$ are

$$J_4^{(a)} = \operatorname{tr}\left[\overline{\boldsymbol{C}}\boldsymbol{M}_{(a)}\right] \qquad \text{and} \qquad J_5^{(a)} = \operatorname{tr}\left[\overline{\boldsymbol{C}}^2\boldsymbol{M}_{(a)}\right] \,. \tag{6}$$

The free energy is split into an isotropic part ψ^{iso} representing the matrix material and two transversely isotropic parts $\psi^{ti}_{(a)}$ for the fibers,

$$\psi(I_1, I_2, I_3, J_4^{(a)}, J_5^{(a)}) = \psi^{iso}(I_1, I_2, I_3) + \sum_{a=1}^{2} \psi^{ti}_{(a)}(I_1, I_2, I_3, J_4^{(a)}, J_5^{(a)}) \,. \tag{7}$$

Obviously we consider the superposition of two transversely isotropic models in order to model the anisotropy of the artery. For the isotropic part the polyconvex and compressible Mooney-Rivlin model

$$\psi^{iso} = c_1 I_1 + c_2 I_2 + c_3 I_3 - \delta \ln \sqrt{I_3} \tag{8}$$

is chosen. When δ is set to $\delta = 2c_1 + 4c_2 + 2c_3$, depending on the three parameters c_1, c_2 and c_3, a stress-free reference configuration is ensured. A widely used function for the transversely isotropic part of the free energy in Eq. (7) which is suitable to describe the strong stiffening effect in fiber direction is given in Holzapfel et al. [2000]:

$$\psi^{ti}_{(a)} = \frac{k_1}{2k_2}\left\{\exp\left[k_2\langle J_4^{(a)} - 1\rangle^2\right] - 1\right\} \quad \text{for} \quad a = 1, 2 \,. \tag{9}$$

The invariant $J_4^{(a)}$ is the square of the stretch in the corresponding fiber direction. The Macaulay bracket $\langle b\rangle := \frac{1}{2}(b + |b|)$ in the latter equation ensures that the fibers will only carry loads if they are elongated, i.e. $J_4^{(a)} > 1$. While k_1 is a stress like parameter, k_2 is dimensionless. For the proof and the benefits accompanied by polyconvexity of the functions in Eq. (8) and Eq. (9) the reader is referred to Schröder and Neff [2003], Schröder

et al. [2005], Balzani et al. [2006] and Schröder [2010]. For the adventitia and the media the parameters were fitted to uniaxial tension tests of human abdominal aortic samples. In these tests the angle $2\beta_f$ between the two considered fiber directions $\boldsymbol{A}_{(1)}$ and $\boldsymbol{A}_{(2)}$ is unknown and was also part of the parameter fitting. To account for the anisotropy, the tension tests of the stripes were carried out in axial and circumferential direction of the artery, see also Balzani et al. [2012b] for details. The parameter adjustment of a variety of polyconvex energy functions can be found in Brands et al. [2008]. Here, the parameters chosen for the adventitia and media are taken from Schröder and Brinkhues [2014], see Table 1. In the numerical examples we will also investigate patient-specific degenerated arteries. The occurring plaque deposits will be assumed to be purely isotropic and homogenous. The investigation of the mechanical properties and hyperelastic modeling is still a research topic of utmost interest. Experimental data on the plaque behavior, see for instance Loree et al. [1994a;b] and Salunke et al. [2001], suffers from the large variance of the results and testing conditions. A review on uniaxial material testing of plaque samples is provided in Walsh et al. [2014], where the authors intended to motivate a more standardized testing protocol. Furthermore, the documented data is not universally valid due to the distinct inhomogeneity of the samples. A review concerning computational aspects of atherosclerotic plaques has recently been published by Holzapfel et al. [2014]. The evolution of atherosclerotic plaque has a strong impact on the mechanical behavior of the whole arterial wall. This was studied in the framework of a sensitivity analysis in Brinkhues et al. [2010] and suitable plaque parameters were assumed, see Table 1.

Table 1: Material parameter sets for different layers.

	ψ_{iso}			$\psi^{(a)}_{\text{aniso}}$		
	c_1 in kPa	c_2 in kPa	c_3 in kPa	k_1 in kPa	$k_2, [k_2] = 1$	β_f in rad
Adventitia	2.326	6.169	60.642	$3.131\ 10^{-8}$	147.174	0.759
Media	14.638	0.149	60.810	6.851	754.014	0.913
Plaque	60.0	15.0	800.0	-	-	-

Based on the free energy function we compute the second Piola-Kirchhoff stress tensor and the Cauchy stress

$$\boldsymbol{S} = 2\frac{\partial \psi}{\partial \boldsymbol{C}} \qquad \text{and} \qquad \boldsymbol{\sigma} = \frac{1}{J}\boldsymbol{F}\boldsymbol{S}\boldsymbol{F}^T \,, \tag{10}$$

respectively. The orientation of the fiber directions in an ideal tube is shown in Fig. 1. Each fiber direction $\boldsymbol{A}_{(a)}$ is inclined by the angle β_f towards the circumferential direction. The angle between the two fiber directions $\boldsymbol{A}_{(1)}$ and $\boldsymbol{A}_{(2)}$ amounts to $2\beta_f$. Note that the angle β_f^{med} of the media and β_f^{adv} of the adventitia are different, compare Table 1.

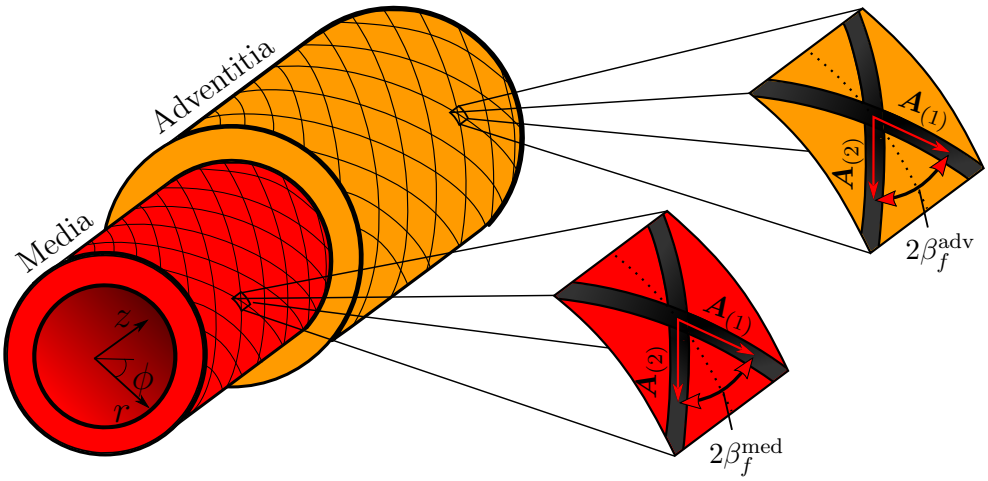

Figure 1: Ideal tube consisting of two material layers with two fiber families each.

3 Algorithmic treatment of residual stresses

The proposed method described in the following is based on the assumption that residual stresses reduce the gradient of the wall stress in radial direction. This hypothesis is motivated by a couple of experimental and numerical studies, see for instance Takamizawa and Hayashi [1987], Chuong and Fung [1986] or Fung [1991]. In a more general context Schröder and Brinkhues [2014] formulated the following hypothesis (here slightly adapted):

The superposition of eigenstresses in arterial walls should decrease the gradient of suitable stress-measures of the final stress state in radial direction. This requirement has to be placed to the individual parts of the arterial wall (e.g. media and adventitia), independently.

Let us consider an ideal cylinder consisting of an inner (media) and an outer (adventitia) layer under internal pressure p_i. The radial stress component will vary continuously from p_i (inner boundary) to zero (outer boundary). The circumferential stresses exhibit in general non-vanishing stress-values at the inner and outer boundaries and could exhibit a jump at the interface between media and adventitia.

The superposition of trial states of eigenstresses will certainly affect the balance of momentum and a new equilibrium placement has to be iterated. Our basic concept is to use local deviations of suitable stress invariants from spatial-sector volume averaged target values for the estimation of the residual stresses.

3.1 Definition of stress measures

Since arterial walls exhibit a distinct material behavior in the fiber directions compared to the directions perpendicular to the fiber, we introduce suitable stress invariants capturing this effect. These invariants in turn will be assumed to be the driving force in the evolution of residual stresses. Such a stress driven criterion is also motivated by experimental findings made by Liu and Fung [1989]. They showed that the opening angle of rat aorta

and therefore the residual stresses significantly correlate with the blood pressure. For the analysis the Cauchy stresses $\boldsymbol{\sigma}$ are additively decomposed into

$$\boldsymbol{\sigma} = \boldsymbol{\sigma}^{*} + \boldsymbol{\sigma}^{\text{reac}} \,, \tag{11}$$

where $\boldsymbol{\sigma}^{*}$ is called ground stress and $\boldsymbol{\sigma}^{\text{reac}}$ is a reaction stress associated to constraints. The idea is to extract the reaction stress from the whole stress tensor. Afterwards, we use the invariants of the reaction stress as additional arguments in our continuum-mechanical framework. The reactions are caused by an assumed inextensibility of the fibers which results in

$$\boldsymbol{\sigma}^{\text{reac}} = T_{(1)}\widetilde{\boldsymbol{m}}_{(1)} + T_{(2)}\widetilde{\boldsymbol{m}}_{(2)} \,. \tag{12}$$

In the following $T_{(1)}$ and $T_{(2)}$ are denoted as the fiber stresses. These invariants will be used as scalar stress measures in order to determine the magnitude of the residual stresses. The tensor

$$\widetilde{\boldsymbol{m}}_{(a)} = \widetilde{\boldsymbol{a}}_{(a)} \otimes \widetilde{\boldsymbol{a}}_{(a)}, \qquad \text{with} \quad a = 1, 2 \tag{13}$$

denotes the spatial structural tensor and is computed with help of the spatial fiber unit direction vector $\widetilde{\boldsymbol{a}}_{(a)}$, using the relations

$$\boldsymbol{a}_{(a)} = \boldsymbol{F}\boldsymbol{A}_{(a)} \,, \qquad \text{and} \qquad \widetilde{\boldsymbol{a}}_{(a)} = \frac{\boldsymbol{a}_{(a)}}{||\boldsymbol{a}_{(a)}||} \,. \tag{14}$$

The additive split in Eq. (11) is complemented by the constraints $\boldsymbol{\sigma} : \widetilde{\boldsymbol{m}}_{(a)} = \boldsymbol{\sigma}^{\text{reac}} : \widetilde{\boldsymbol{m}}_{(a)}$, i.e. $\boldsymbol{\sigma}^{*}$ has to satisfy

$$\boldsymbol{\sigma}^{*} : \widetilde{\boldsymbol{m}}_{(1)} = 0 \qquad \text{and} \qquad \boldsymbol{\sigma}^{*} : \widetilde{\boldsymbol{m}}_{(2)} = 0 \,. \tag{15}$$

The proposed setup and the invariant definition according to convenient constraints is motivated by the ideas of Mulhern et al. [1967] and Spencer [1972] concerning elastoplasticity. First of all the projections of the Cauchy stress onto the current preferred directions are given by

$$\begin{aligned} \boldsymbol{\sigma} : \widetilde{\boldsymbol{m}}_{(1)} &= T_{(1)} + T_{(2)}\widetilde{\boldsymbol{m}}_{(1)} : \widetilde{\boldsymbol{m}}_{(2)} \,, \\ \boldsymbol{\sigma} : \widetilde{\boldsymbol{m}}_{(2)} &= T_{(1)}\widetilde{\boldsymbol{m}}_{(2)} : \widetilde{\boldsymbol{m}}_{(1)} + T_{(2)} \,. \end{aligned} \tag{16}$$

Solving the above system of equations for the fiber stress invariants $T_{(1)}$ and $T_{(2)}$ in an arbitrary deformation state leads to the formulas

$$\begin{aligned} T_{(1)} &= \frac{\boldsymbol{\sigma} : \widetilde{\boldsymbol{m}}_{(1)} - \boldsymbol{\sigma} : \widetilde{\boldsymbol{m}}_{(2)}\xi}{1 - \xi^2} \quad \text{and} \\ T_{(2)} &= \frac{\boldsymbol{\sigma} : \widetilde{\boldsymbol{m}}_{(2)} - \boldsymbol{\sigma} : \widetilde{\boldsymbol{m}}_{(1)}\xi}{1 - \xi^2} \,, \end{aligned} \tag{17}$$

with the abbreviation $\xi = \widetilde{\boldsymbol{m}}_{(1)} : \widetilde{\boldsymbol{m}}_{(2)}$. In the former version of Schröder and Brinkhues [2014] the reaction stresses $\boldsymbol{\sigma}^{reac}$ contained the additional term $-p\mathbf{1}$. These hydrostatic stresses obviously also include radial stress components. As already discussed above, for an ideal cylinder the radial stresses at the inner and outer boundary are already predefined through the equilibrium condition. Likewise at the media-adventitia interface Γ the radial stresses have to coincide. Therefore, if we aim to estimate a residual stress tensor based on $\boldsymbol{\sigma}^{reac}$ it is constructive to preclude p in its definition. Further it was found that the novel setup increases the robustness of the algorithm, especially in case of 3D-applications. In so far the definition of the reaction stresses in Eq. (12) was changed compared to Schröder and Brinkhues [2014]. In this preliminary work it was assumed that $\text{tr}\boldsymbol{\sigma}^{\text{res}} = 0$ which allowed to determine the hydrostatic pressure p.

3.2 Engineering based procedure to estimate a residual stress tensor

The estimation of the residual stresses is accomplished within an iterative process. Based on the aforementioned relations and assumptions a calculation procedure to account for residual stresses is explained. The complete geometry may be divided into a finite number of $\mathrm{n_{SC}}$ sectors. Each of these sectors has an assigned domain

$$\mathcal{B}^{\measuredangle,\mathrm{mat}} = \{\mathcal{B}^{\measuredangle,\mathrm{media}},\ \mathcal{B}^{\measuredangle,\mathrm{adventitia}}\}\ , \tag{18}$$

see also Fig. 2. After incrementally loading the artery with the internal blood pressure and solving the balance of momentum, the Cauchy stresses $\boldsymbol{\sigma}$ and the deformation gradient $\boldsymbol{F}$ are given. The residual stresses are directly estimated from the current stress state. The "loading" of the system with the residual stresses is performed in so called smoothing-loops, which are to be repeated until an adequately flat stress distribution is reached. In each assigned sector domain $\mathcal{B}^{\measuredangle,\mathrm{mat}}$ the mean fiber stresses $\overline{T}_{(a)}^{\measuredangle,\mathrm{mat}}$ can be calculated. These are averaged over the spatial sector volume $v^{\measuredangle,\mathrm{mat}}$:

$$\overline{T}_{(a)}^{\measuredangle,\mathrm{mat}} = \frac{1}{v^{\measuredangle,\mathrm{mat}}} \int\limits_{\mathcal{B}^{\measuredangle,\mathrm{mat}}} T_{(a)}(\boldsymbol{x})\ \mathrm{d}v \quad \text{for } \mathcal{B}^{\measuredangle,\mathrm{mat}} = \{\mathcal{B}^{\measuredangle,\mathrm{media}}, \mathcal{B}^{\measuredangle,\mathrm{adventitia}}\}\ . \tag{19}$$

The physical pertinence of the averaging procedure over the spatial segments is increased by decreasing the segment angles α and when the variation of the preferred direction within the considered segment is small. The subtraction of the mean values from the local fiber stresses, see Eq. (17), yields the local deviations

$$\Delta T_{(a)} = T_{(a)} - \overline{T}_{(a)}^{\measuredangle,\mathrm{mat}} \quad \text{for} \quad \mathcal{B}^{\measuredangle,\mathrm{mat}} = \{\mathcal{B}^{\measuredangle,\mathrm{media}},\ \mathcal{B}^{\measuredangle,\mathrm{adventitia}}\}\ . \tag{20}$$

The deviation of the residual stress tensor

$$\Delta\boldsymbol{\sigma}^{\mathrm{res}} = \sum_{a=1}^{2} \Delta T_{(a)}\, \widetilde{\boldsymbol{m}}_{(a)} \tag{21}$$

is approximated by using Eq. (12) and the computed fiber stress deviations in Eq. (20). In view of the algorithmic treatment the total residual stresses will be updated incrementally. This is facilitated in a sub-incrementation within n_{inc} steps until the total proportionate factor $\gamma \in [0,1]$ is applied:

$$\boldsymbol{\sigma}^{\mathrm{res}} \Leftarrow \boldsymbol{\sigma}^{\mathrm{res}} + \frac{\gamma}{n_{\mathrm{inc}}} \Delta\boldsymbol{\sigma}^{\mathrm{res}}\ ,\ \text{where } \gamma \in [0,1]\ . \tag{22}$$

In order to incorporate the updated residual stress tensor

$$\boldsymbol{S}^{\mathrm{res}} = J\boldsymbol{F}^{-1}\boldsymbol{\sigma}^{\mathrm{res}}\boldsymbol{F}^{-T} \tag{23}$$

in the reference configuration is computed. Finally, the residual stresses $\boldsymbol{S}^{\mathrm{res}}$ are superposed, i.e. they are subtracted from the stresses $\boldsymbol{S}^{*}$, see Eq. $(10)_1$:

$$\boldsymbol{S} = \boldsymbol{S}^{*}\left(\overline{\boldsymbol{C}}, \boldsymbol{M}_{(a)}\right) - \boldsymbol{S}^{\mathrm{res}} \quad \text{with} \quad \boldsymbol{S}^{*} = 2\frac{\partial\psi\left(\overline{\boldsymbol{C}}, \boldsymbol{M}_{(a)}\right)}{\partial\boldsymbol{C}}\ . \tag{24}$$

After that a new equilibrium state has to be iterated, where $\boldsymbol{S}^{\mathrm{res}}$ is treated as constant. The smoothing-loops can be repeated several times and a stopping criterion has to be

defined. The easiest way would be to compare the maximum and minimum of $T_{(a)}$ in each sector and to stop smoothing, when the difference is small. A more sophisticated way could be to evaluate the norm of the spatial gradient of $T_{(a)}$ and stop when $||\text{Grad}T_{(a)}||$ becomes smaller than a certain tolerance value, which still needs to be chosen. The factor γ was introduced in order to apply only a fraction of the residual stresses within the considered load increment. After each update of $\boldsymbol{\sigma}^{\text{res}}$ the residual stresses are stored as history variables. When iterating a new equilibrium state the residual stresses remain unaltered, while $\boldsymbol{S}^*\left(\overline{\boldsymbol{C}}, \boldsymbol{M}_{(a)}\right)$ changes until the weak form of balance of linear momentum is fulfilled.

Figure 3 illustrates qualitatively the idea of the proposed procedure. It shows a schematic plot of the fiber stress invariant distribution over the radial direction $\tilde{r} \in [r_i, r_a]$ with the inner radius r_i and the outer radius r_a. The jump of $T_{(a)}$ (which can roughly be interpreted as circumferential stress quantities) in radial direction across the material interface Γ is characteristic because of the difference in stiffness provided by the media and adventitia.

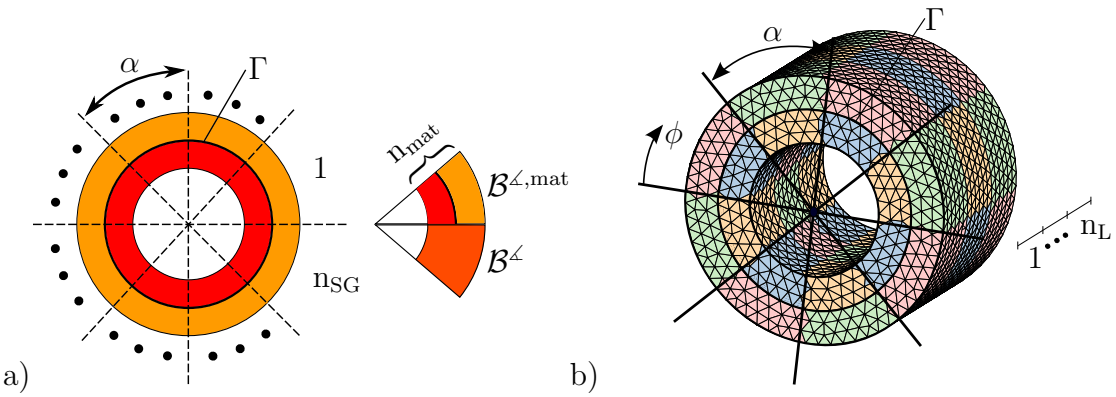

Figure 2: a) Decomposition of an arterial cross-section, consisting of two materials n_{MAT} (media (red) and adventitia (orange)) into 8 segments n_{Sg} and $\text{n}_{\text{SC}}^{\text{2D}} = \text{n}_{\text{SG}} \cdot \text{n}_{\text{MAT}} = 16$ sectors and b) additional longitudinal decomposition in $\text{n}_{\text{L}} = 3$ parts giving $\text{n}_{\text{SC}}^{\text{3D}} = \text{n}_{\text{SC}}^{\text{2D}} \cdot \text{n}_{\text{L}} = 48$ sectors.

The computation of the mean values $\overline{T}_{(a)}^{\angle,\text{mat}}$ is carried out on sector domains $\mathcal{B}^{\angle,\text{mat}}$. The decomposition of the artery into a number of $\text{n}_{\text{SC}}^{\text{3D}}$ is to be demonstrated along with Fig. 2. By specification of an angle α the exemplary cross-section with two material layers in a) is decomposed into $n_{\text{SG}} = 8$ segments. For the division into segments the centroid of the lumen is utilized as indicated in Fig. 2b). Then for each finite element the center coordinates are computed. A segment number is assigned if the magnitude of the polar angle ϕ of the center coordinate is in between the polar angles of the segment borders. That means all Gauss-Points of one element belong to the same segment, i.e. the segments do not intersect elements. Each segment got an angle $\alpha = 360°/n_{\text{SG}}$.

The subdivision of the segment domain $\mathcal{B}^{\angle}$ into sector domains $\mathcal{B}^{\angle,\text{mat}}$ is performed with respect to the material layer and the interface Γ, see Fig. 2a). The consideration of three-dimensional numerical simulations requires an additional decomposition in longitudinal direction, compare Fig. 2b). The total number of sectors of a three-dimensional geometry is defined by

$$\text{n}_{\text{SC}}^{\text{3D}} = \text{n}_{\text{SG}} \cdot \text{n}_{\text{mat}} \cdot \text{n}_{\text{L}} \tag{25}$$

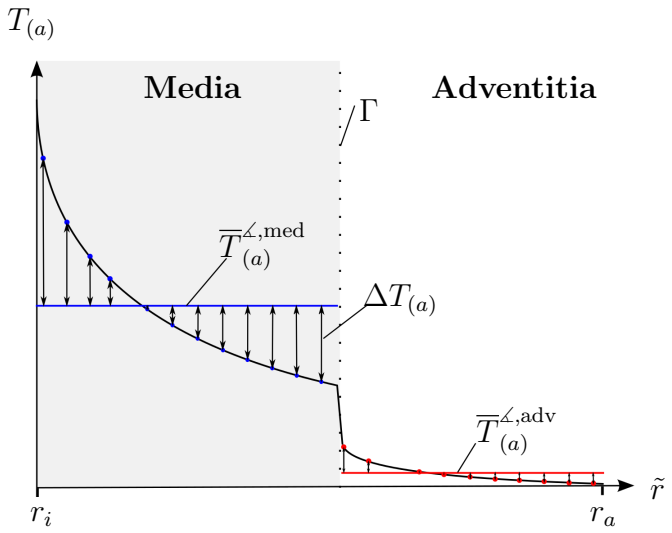

Figure 3: Exemplary fiber stress distribution over the wall thickness and corresponding deviations $\Delta T_{(a)}$ with respect to the segmental mean stresses $\overline{T}^{\angle,\mathrm{mat}}_{(a)} = \{\overline{T}_{(a)}{}^{\angle,\mathrm{media}}, \overline{T}_{(a)}{}^{\angle,\mathrm{adventitia}}\}$.

with the number of segments n_{SG}, the number of material layers n_{mat} and the number of longitudinal segments n_{L}. Table 2 summarizes the described algorithmic treatment in a compact form.

- Divide domain $\mathcal{B}$ into $\mathrm{n}^{\mathrm{2D}}_{\mathrm{SC}}$ or $\mathrm{n}^{\mathrm{3D}}_{\mathrm{SC}}$ sectors, initialize $\boldsymbol{\sigma}^{\mathrm{res}} = \mathbf{0}$
- Apply internal pressure p_{i} (incrementally) and solve the nonlinear boundary value problem: Compute $\boldsymbol{F}, \boldsymbol{S}$
- DO number of smoothing loops (n_{SL})
  - a) $\boldsymbol{\sigma} = \boldsymbol{F}\,\boldsymbol{S}\,\boldsymbol{F}^T/J$, $\widetilde{\boldsymbol{m}}_{(a)}$ and $T_{(a)}$
  - b) local volume average of fiber-stresses $\overline{T}^{\angle,\mathrm{mat}}_{(a)}$, Eq. (19)
  - c) deviations $\Delta T_{(a)}$, Eq. (20)
  - d) residual stresses $\Delta\boldsymbol{\sigma}^{\mathrm{res}}$, Eq. (21)
  - e) DO number of sub-incrementation loops (n_{inc})
    - $\boldsymbol{\sigma}^{\mathrm{res}} \Leftarrow \boldsymbol{\sigma}^{\mathrm{res}} + \frac{\gamma}{n_{\mathrm{inc}}}\Delta\boldsymbol{\sigma}^{\mathrm{res}}$, $\gamma \in [0,1]$
    - $\boldsymbol{S}^{\mathrm{res}} = J\boldsymbol{F}^{-1}\boldsymbol{\sigma}^{\mathrm{res}}\boldsymbol{F}^{-T}$
    - $\boldsymbol{S} = \boldsymbol{S}^*\left(\overline{\boldsymbol{C}}, \boldsymbol{M}_{(a)}\right) - \boldsymbol{S}^{\mathrm{res}}$, with $\boldsymbol{S}^*$ from Eq. $(10)_1$
    - Solve balance of linear momentum: Compute $\boldsymbol{F}, \boldsymbol{S}$

  END DO

END DO

sub-incrementation

smoothing-loop

Table 2: Algorithmic box for the computation of the residual stresses.

4 Three-dimensional numerical simulations

4.1 Numerical simulation of a tube

As a first academical example we consider an ideal tube consisting of media and adventitia, while the intima is neglected. The specific boundary value problem is shown in Figure 4. The inner radius is $r_i = 1.0$ mm and the outer radius $r_a = 2.0$ mm. Both layers have a thickness of 0.5 mm and the sample is 1 mm long. In order to enforce plane strain like conditions the arterial wall is fixed at both ends in x_3-direction and on two single nodes. When estimating the opening angle the tube is allowed to deform in x_3-direction in order to release the axial residual stresses and the mesh is cut on one side of the artery in order to release the circumferential residual stresses. The tube is initially loaded with an internal pressure p_i of 16 kPa which corresponds to 120 mmHg.

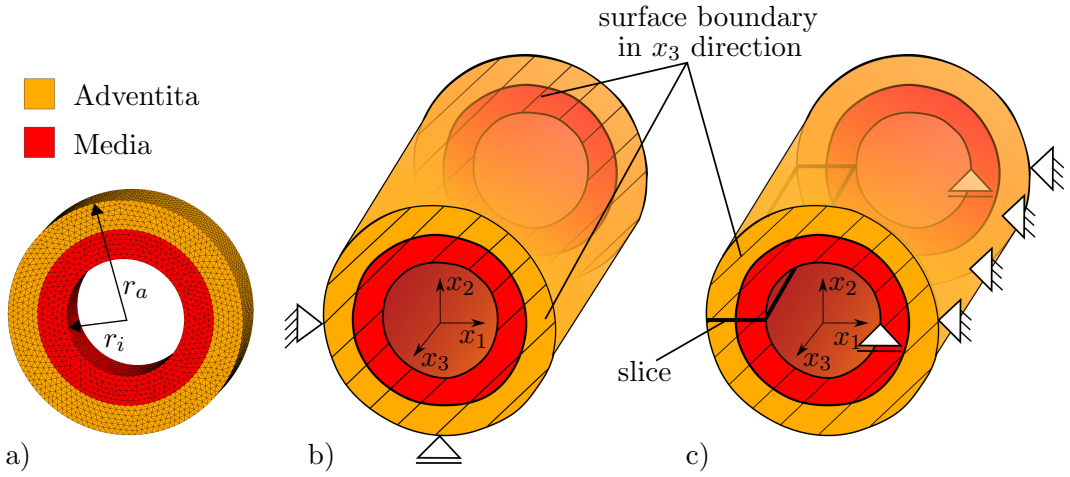

Figure 4: a) Three-dimensional tube discretized with 69 621 quadratic, standard elements and boundary conditions of b) the in vivo problem and c) the opening angle experiment.

In this special case the decomposition into only two sectors - one for the media and one for the adventitia - is sufficient due to the rotational symmetry of the fiber orientation and the considered body. In Fig. 5 and Fig. 6 the stresses in the Gauss-points in the x_1-x_3 plane are evaluated and the stress distributions before and after smoothing are to be compared. For the stress plots the Gauss-points in the plane were meshed with help of a *Delaunay triangulation*. Then the corresponding stresses are plotted on the perpendicular x_2-axis. In this section σ_{11}, σ_{22} and σ_{33} represent the radial (σ_r), circumferential (σ_φ) and longitudinal stresses. After application of ten smoothing-loops ($n_{SL} = 10$) with $n_{inc} = 1$ and a proportionate factor γ of 100% the fiber stress invariant $T_{(1)}$ becomes nearly constant in each material layer, see Fig. 5. The high stress gradient, especially in the area close to the lumen interface vanishes. For the considered ideal tube and the underlying fiber orientation the second invariant $T_{(2)}$ is identical to $T_{(1)}$. The difference of the radial stress distribution before and after smoothing is comparatively small. The circumferential and longitudinal stress distributions are depicted in Fig. 6. In general the main observations made for the fiber stress invariant $T_{(1)}$ also hold for the circumferential stresses σ_φ and longitudinal stresses σ_{33}. Overall, the presented algorithm seems to be well suited to realize the fundamental hypothesis made at the beginning.

The improvement of the modification in the definition of the anisotropic invariants $T_{(1)}$

and $T_{(2)}$ becomes apparent when comparing Fig. 5 and Fig. 7. The results of the old approach, depicted in Fig. 7 reveal considerable stress oscillations for σ_r, although $T_{(1)}$ becomes sufficiently even. As already described at the end of section 3.1 the incorporation of relatively large radial stresses, which are not really physical due to the stress constraints, is supposed to be responsible for that. This effect did not occur in 2D calculations. Note that the fiber stress $T_{(1)}$ in Fig. 5a) and Fig. 7a) before smoothing are different due to the modified ansatz.

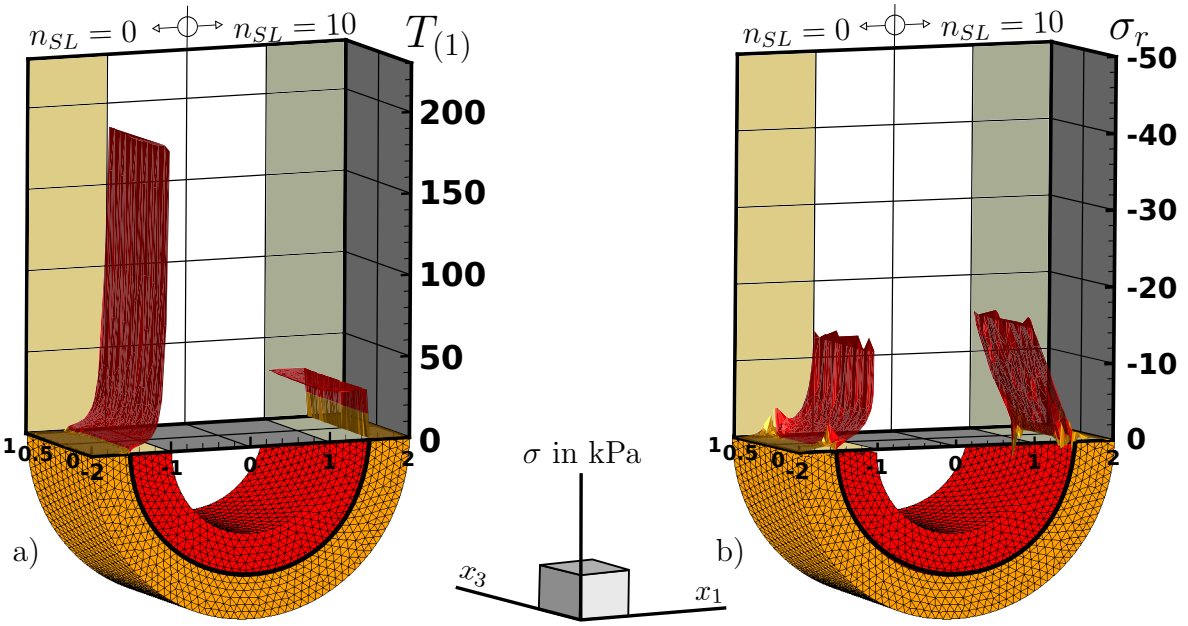

Figure 5: Gauss-point plots of the distribution of a) the fiber stress $T_{(1)}$ and b) the radial stress σ_r. Stress distributions without residual stresses (left part of each figure) and after application of 10 smoothing loops (right part of each figure) are compared.

In order to analyze the opening characteristics of the artery due to the determined residual stresses the sliced configurations are loaded with $\boldsymbol{S}^{\text{res}}$ on the Gauss-point level in the absence of any external forces. On that basis the simulation provides an additional, layer specific tool to judge whether the approach is in good accordance with available experimental observations. Different simulations of the opening angles are shown in Fig. 8. In detail, it contains the opening angles of the complete artery, the single adventitia and the single media, where the volume averaged global target values were computed on the sector domains $\mathcal{B}^{\measuredangle,\text{mat}}$, compare also Fig. 2. Experimental data regarding the opening angles of separated arterial layers is provided in Holzapfel et al. [2007]. Consequently, Holzapfel and Gasser [2007] and Holzapfel and Ogden [2010] also considered different opening angles, when deducing residual strains from opening angle experiments. The opening angle of the media is largest for the media followed by the complete artery and the adventitia, which is in accordance with experimental findings in Holzapfel et al. [2007]. However, the remaining von Mises stresses $\sigma_{\text{vM}} = \sqrt{3/2\ \text{Dev}\boldsymbol{\sigma} : \text{Dev}\boldsymbol{\sigma}}$ in the opened complete artery (Fig. 8, left column) are considerably higher compared to the opened adventitia (Fig. 8, middle column) and opened media (Fig. 8, right column). Essential to determine the magnitude of the residual stresses are the fiber stress deviations from the mean values, see

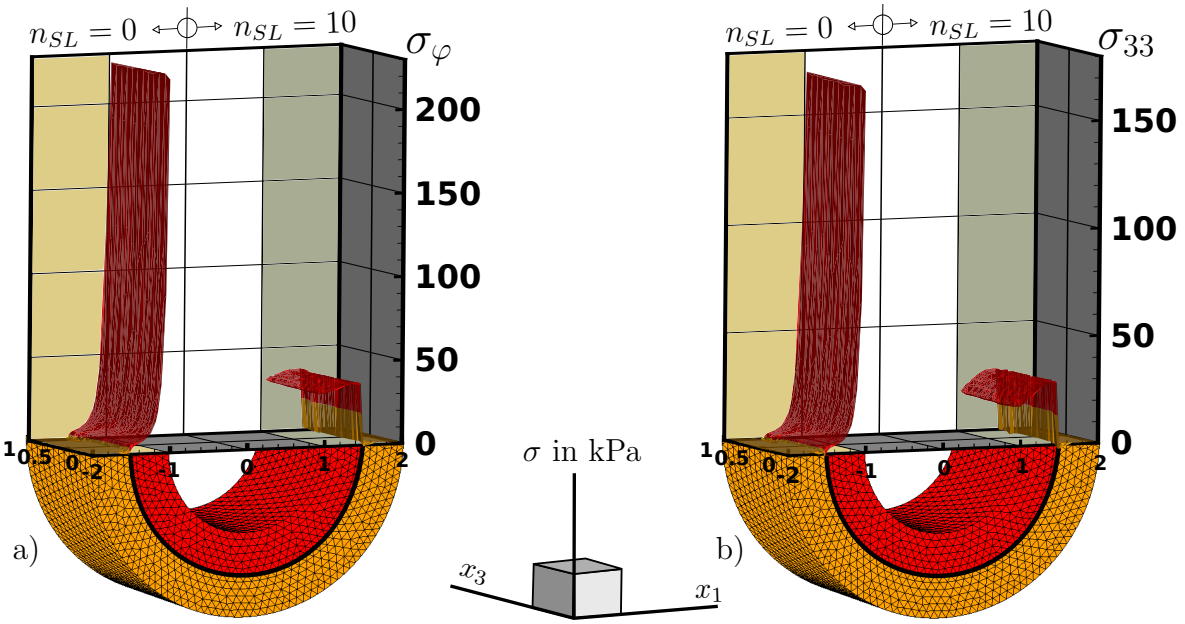

Figure 6: Gauss-point plots of the distribution of a) the circumferential stress σ_φ and b) the longitudinal stress σ_{33}. Stress distributions without residual stresses (left part of each figure) and after application of 10 smoothing loops (right part of each figure) are compared.

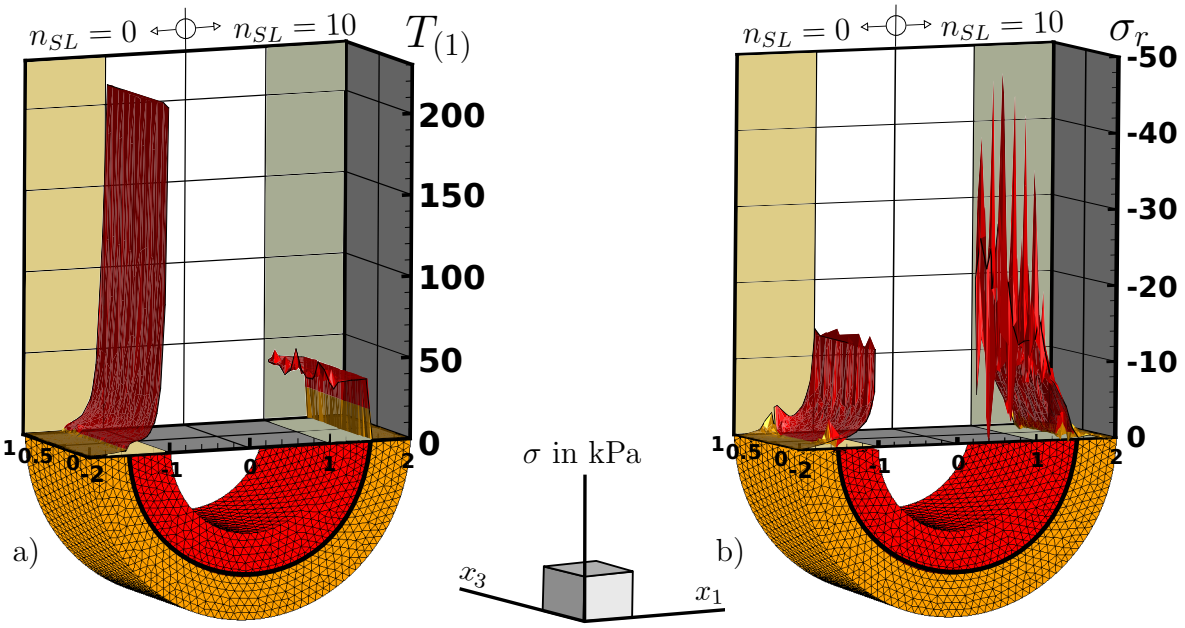

Figure 7: Gauss-point plots of the distribution of a) the fiber stress $T_{(1)}$ and b) the radial stress σ_r for the preliminary fiber invariant construction in Schröder and Brinkhues [2014]. Stress distributions without residual stresses (left part of each figure) and after application of 10 smoothing loops (right part of each figure) are compared old Approach.

Eq. (20). Fig. 9a) shows the stress distribution in a cross-section through the vessel wall after zero smoothing-loops ($n_{SL} = 0$), i.e. when only the internal pressure p_i is acting. Moreover, it includes the plots after application of one, two and five smoothing loops with a proportionate factor γ of 100%. The corresponding mean values are plotted in Fig. 9b). After five loops the distributions of $T_{(1)}$ and $\overline{T}^{\measuredangle,\mathrm{mat}}_{(1)}$ are approximately equal. Generally the deviations $\Delta T_{(a)}$ on both layers lead to a bending dominated problem. Obviously the deviations on the adventitia are a lot smaller compared to the media. Consequently the opening angle of the adventitia is smaller.

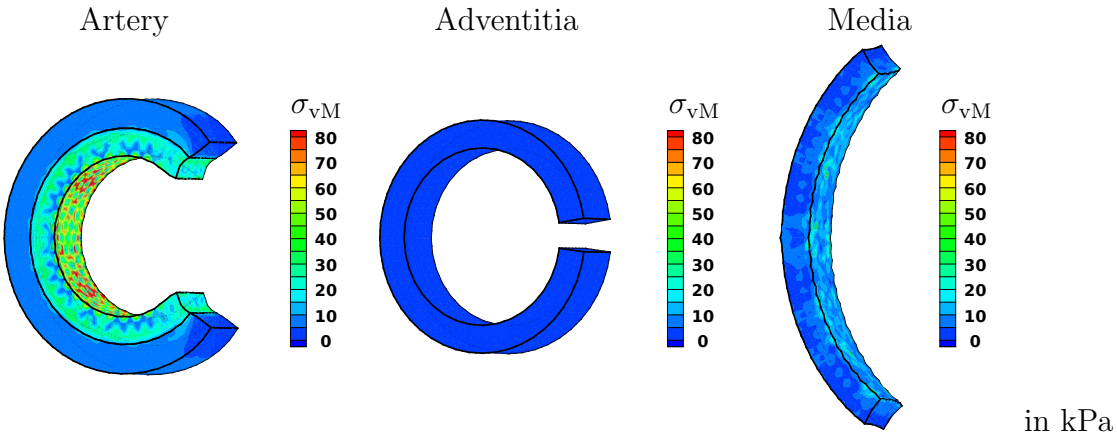

Figure 8: Simulations of the opening angle for the complete artery, the single adventitia and the single media after five smoothing-loop with $\gamma = 100\%$. The contour plots depict the von Mises stresses σ_{vM}.

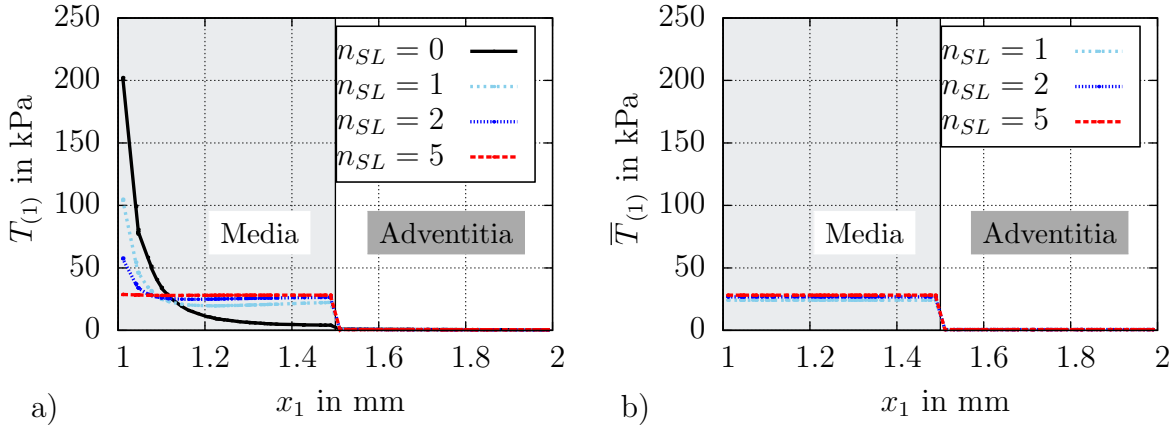

Figure 9: a) Fiber stress distribution over the radius after zero, one, two, and five smoothing loops and b) corresponding mean values.

4.2 Numerical simulation of patient-specific arteries

4.2.1 The influence of residual stresses on the final stress distribution. In this section the proposed approach is applied to three-dimensional simulations of coronary patient-specific arterial walls. The arterial geometries are reconstructed based on two sequenced two-dimensional *virtual histology (VH) intravascular ultrasound (IVUS)* images.

This method is catheter based and provides a series of grey-scale images which allows to identify the lumen and the media-adventitia interface.

Since IVUS images are unable to determine the boundary of the adventitia and the surrounding connective tissue the thickness of the adventitia is chosen appropriately. This is facilitated by computing the centroid of the media-adventitia interface and scaling the radius of each interface point by a factor of 1.15. The resulting line is defined to be the interface between the adventitia and the surrounding connective tissue. Due to the low stiffness provided by the adventitia in case of physiological loading conditions, the associated thickness is assumed to be of minor importance. Accompanied by the assumption that the residual stress state is dominated by the media, cf. Badel et al. [2012], we will perform the averaging of the stress measures on the sector domains $\mathcal{B}^{\measuredangle,\mathrm{mat}}$ in the following examples. VH IVUS also provides color-coded images which allow to determine the different plaque constituents of atherosclerotic arteries and its shape. For a detailed description of the three-dimensional reconstruction the reader is referred to Balzani et al. [2012a].

The plaque is modeled as a homogenous, isotropic body and no residual stresses are computed for this part of the artery. In the first example we consider the geometry depicted in Fig. 10, where the plaque is shown on the left. The model is discretized with 29 063 mixed elements with quadratic shape functions for the displacements and constant volume dilation. In order to study the influence of the sector size we distinguish a decomposition into $\mathrm{n}_{\mathrm{SC}}^{\mathrm{3D}} = 1 \cdot 2 \cdot 1 = 2$ and $\mathrm{n}_{\mathrm{SC}}^{\mathrm{3D}} = 20 \cdot 2 \cdot 3 = 120$ sectors. Since we consider the adventitia and the media for the computation of the residual stresses we have $\mathrm{n}_{\mathrm{MAT}} = 2$. In the first case the whole adventitia and the whole media define a sector, each. As already mentioned a segmentation in longitudinal direction is also possible. In the second case the arterial segment is further divided into $\mathrm{n}_{\mathrm{L}} = 3$ parts in this direction. The marked sections A-A and B-B will be used to evaluate and illustrate the stress distributions.

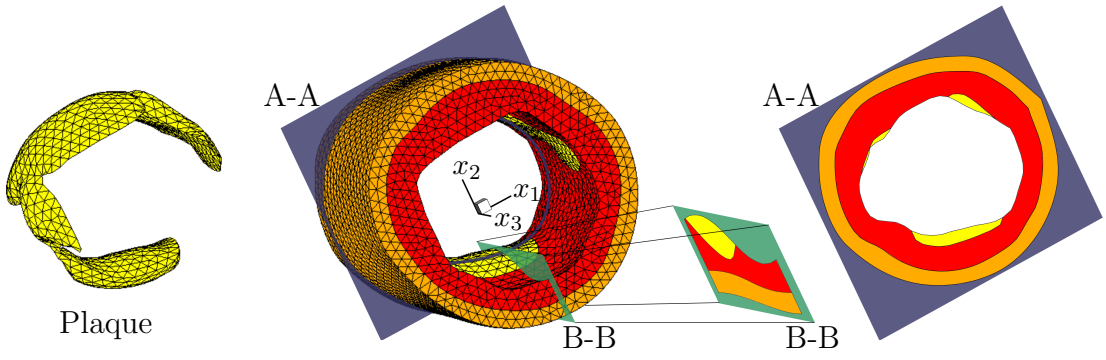

Figure 10: Reconstructed degenerated patient-specific arterial wall, discretized with 29 063 elements and definition of the sections A-A and B-B.

Again the simulation begins with the loading of the stress free arterial wall with an internal pressure of $p_i = 16$ kPa. Thereafter, a number of smoothing-loops is applied, each with an amount of $\gamma = 50\%$. A comparison of the first fiber stress invariant $T_{(1)}$ is depicted in Fig. 11 for the case that no residual stresses are considered and after the application of one and five smoothing-loops. It is visible that the residual stresses influence the stress distribution in the physiological loading range such that the chosen stress measure is

smoothed. The difference between the computations with 2 and 120 sectors is relatively small. Nevertheless, the finer partition seems to reduce the stress gradient slightly more effective. More important in that context is to mention that the coarse partition needed additional sub-incrementation loops (compare Table 2) to guarantee convergence. In case of the fine division with 120 sectors only one sub-incrementation loop ($n_{inc} = 1$) was required in each smoothing loop.

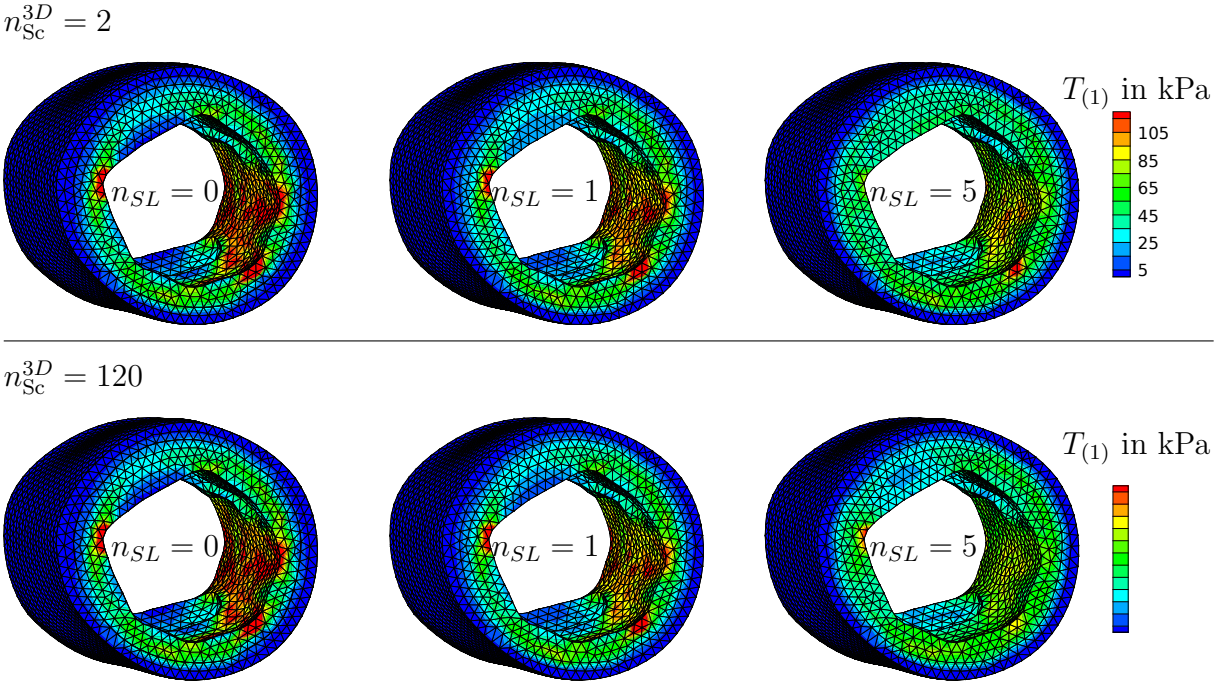

Figure 11: Contour plot of the first fiber stress invariant $T_{(1)}$ after 0, 1 and 5 performed smoothing-loops with $\gamma = 50\%$ for $n_{\mathrm{Sc}}^{3D} = 2$ and $n_{\mathrm{Sc}}^{3D} = 120$, respectively.

The same observation is made for the second fiber stress invariant $T_{(2)}$ in section A-A, see Fig. 12. With an increasing number of smoothing-loops the stress distribution becomes more uniform. Because of the assumption that the plaque is isotropic the plaque was excluded from both fiber invariant plots. The main underlying hypothesis of the proposed scheme was that residual stresses smooth the stress gradient of suitable stress measures. In section B-B the stresses σ_{11} corresponding to the x_1 axis in Fig. 14 approximates the circumferential stresses, see Fig. 13. Again with an increasing number of smoothing-loops the stresses are homogenized and the main assumption implied in the hypothesis is fulfilled. Especially in this section the performance of the fine parition seems to be superior regarding the hypothesis.

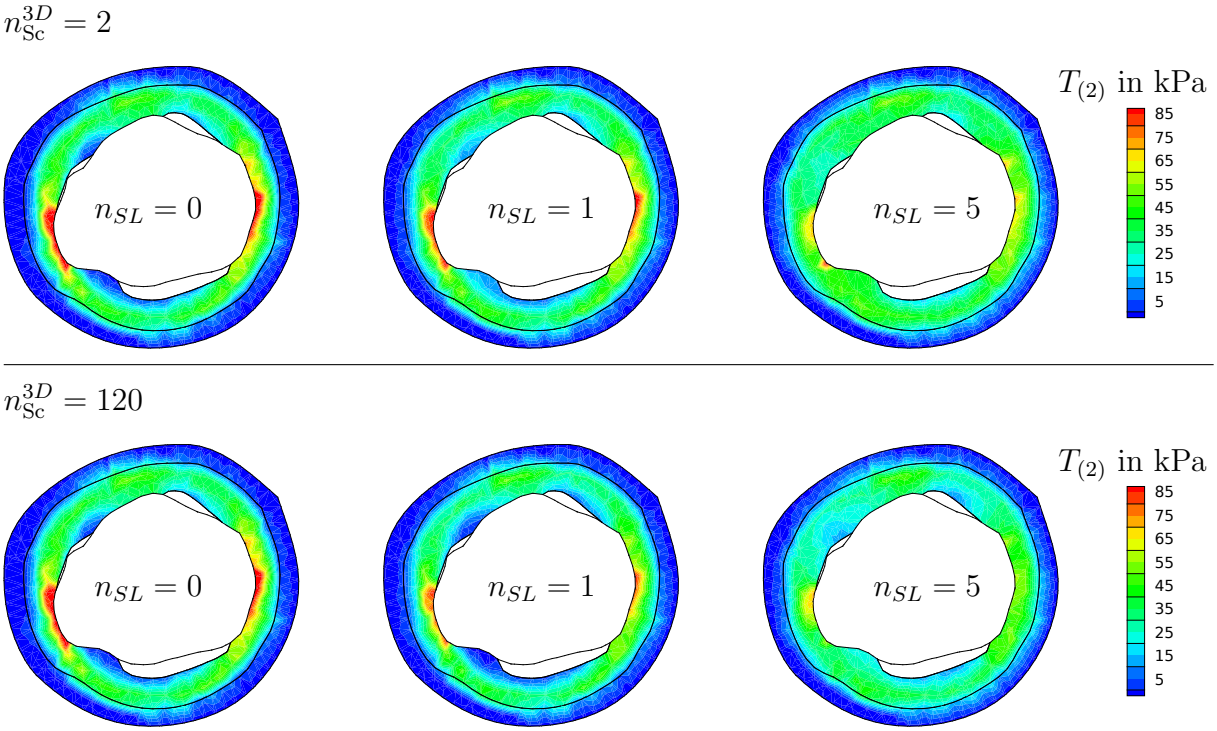

Figure 12: Contour plot of the second fiber stress invariant $T_{(2)}$ in section A-A after 0, 1 and 5 performed smoothing-loops with $\gamma = 50\%$ for $n_{\mathrm{Sc}}^{3D} = 2$ and $n_{\mathrm{Sc}}^{3D} = 120$, respectively.

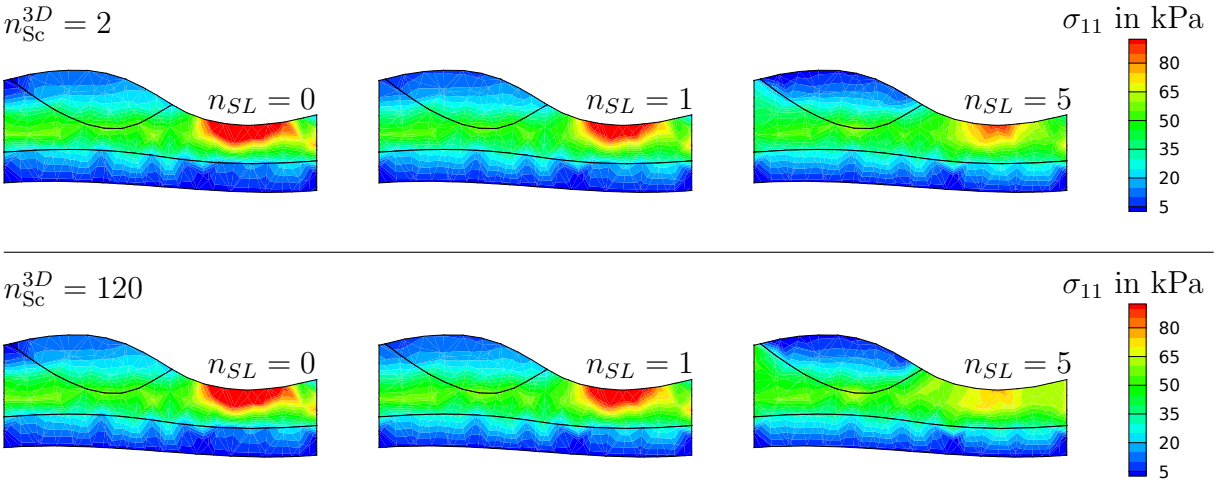

Figure 13: Contour plot of the stresses σ_{11} in section B-B after performing 0, 1 and 5 smoothing-loops with $\gamma = 50\%$ for $n_{\mathrm{Sc}}^{3D} = 2$ and $n_{\mathrm{Sc}}^{3D} = 120$, respectively.

4.2.2 Prediction of the opened configuration. As a second example we consider the geometry depicted in Fig. 14. As outlined in the introduction, the opening angle is a sensitive measure and depends on multiple factors. Therefore, one of the main goals is to provide an engineering tool which is able to be adjusted, such that given experiments can be reproduced. The parameters to be optimized in that case would be γ and n_{SL}. The body is discretized with 26 234 mixed elements with quadratic shape functions for the displacements and constant volume dilation. The plaque deposit is more pronounced in this case and we want to investigate the opened configuration of the media. Therefore three different radial slices are analyzed.

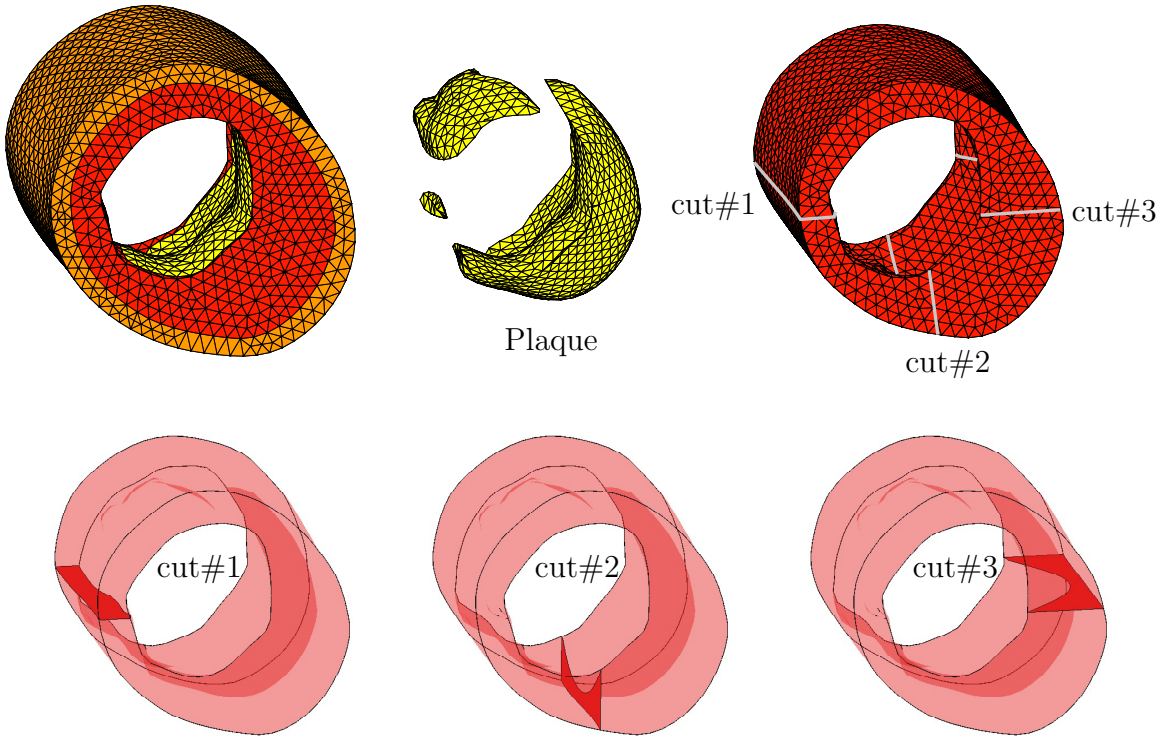

Figure 14: Reconstructed degenerated patient-specific arterial wall, discretized with 26 234 elements and definition of three different cuts on the media.

For cut#1 the opened configuration after different amounts of smoothing-loops are compared in Fig. 15. Naturally, the opening expands, when γ or the number of loops n_{SL} is increased. The same holds for the remaining, unreleased stresses. Generally, the reduction of γ may help to improve the convergence, since the change in $\boldsymbol{\sigma}^{\text{res}}$ is reduced, see Eq. (22). A proportionate factor of 100%, as applied on the ideal artery in 4.1, was found to be ineffective and numerically unstable. In the present example we see that the increase in the deformation from $n_{SL} = 2,\ \gamma = 0.5$ to $n_{SL} = 3,\ \gamma = 0.5$ is almost invisible, i.e. further smoothing loops would not lead to an increase in the deformation because the stress gradient, and therefore $\Delta\boldsymbol{\sigma}^{\text{res}}$, already became small.

Ensuring comparability of the opened configurations, all different slices are evaluated for $n_{SL} = 2$ and $\gamma = 50\%$. The comparison of the opened configuration of all three cuts is shown in Fig. 16. Obviously, the displacements are significantly larger for cut#2 and cut#3. One reason is most probably that the plaque is free of residual stresses. On the other hand in the region of large plaque deposits and a thickened vessel the wall

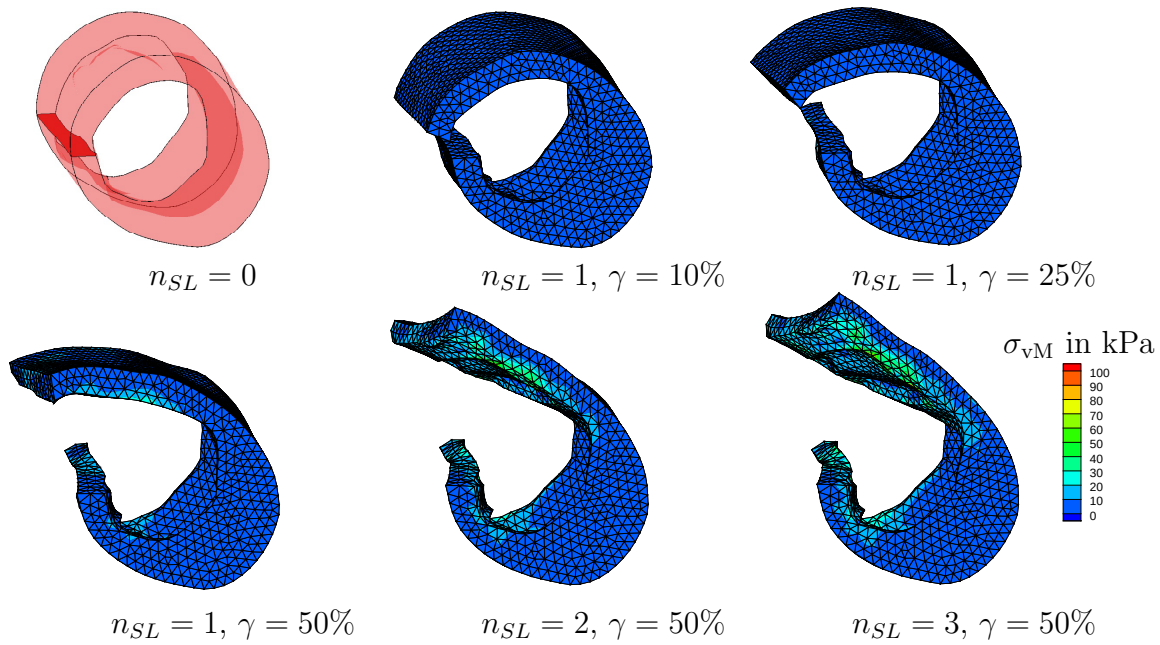

Figure 15: Opened configurations of the media for cut#1 after different amounts of smoothing-loops and proportionate factors.

stress of the media is considerably reduced, see also Fig. 11-13. However, for a patient-specific artery the opened configuration and the stress release may be highly dependent on the position of the slice. This seems reasonable since it is well known that during lifetime arteries adapt to external influences by growth and remodeling processes. It also coincides with the experimental observation made by Liu and Fung [1989] that residual stresses change rapidly and remarkably due to change in blood pressure.

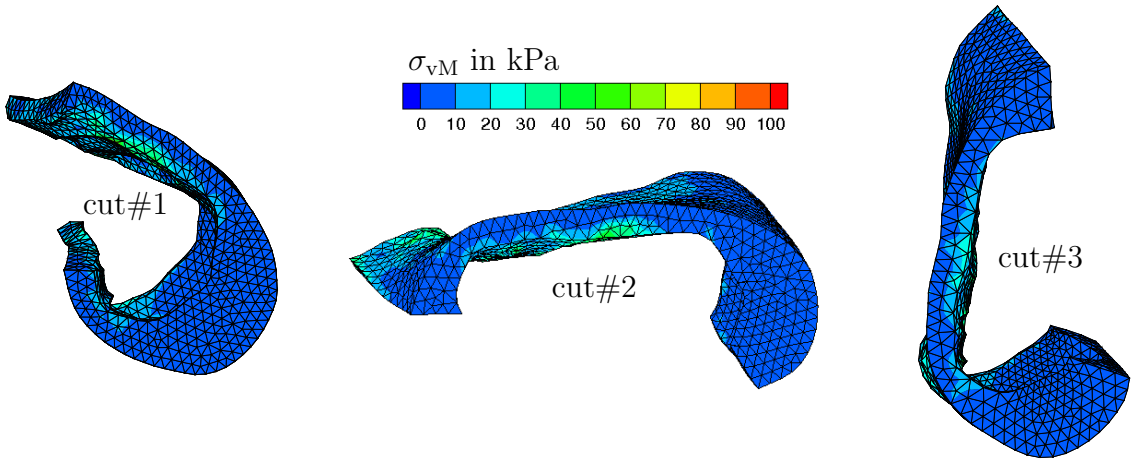

Figure 16: Opened configurations of the media for three different cuts after two smoothing-loops with $\gamma = 50\%$.

The authors are well aware that the IVUS VH images are captured in-vivo. Therefore, only the deformed actual geometries are known. This fact was neglected in the presented examples. Nevertheless, the discussed scheme can easily be adapted to the inverse mod-

eling finite element formulation developed by Govindjee and Mihalic [1996], where the deformed configuration and current loads are known and the unknown reference configuration is computed. In their formulation the weak form of the balance of momentum is parametrized in terms of the inverse motion $\boldsymbol{\varphi}^{-1}$ and its linearization is performed. Here, the algorithm can easily be adjusted to estimate a residual stress tensor in the described way. The inverse finite element concept was also extended to three-field functionals for quasi incompressible problems, see Govindjee and Mihalic [1998] and Liu et al. [2007]. Likewise, the method developed in Gee et al. [2010], which is based on a modified updated Lagrangian formulation, could be adapted to account for residual stresses.

5 Summary

In this contribution we proposed an engineering approach to estimate residual stresses in patient-specific arteries. The residual stresses are directly deduced from the current stress state which is determined based on the equilibrium placement of the artery under blood pressure. The experimentally motivated hypothesis was to smooth the gradients of suitable stress measures. These in turn were derived and sector wise volume averaged mean values were introduced in order to define target values. The smoothing procedure itself can be performed individually for different material layers and is embedded in an iterative numerical scheme. Due to the choice of fiber stress invariants, depending on the well defined fiber directions the procedure is carried out in a coordinate-invariant setting, i.e. we are not restricted by e.g. polar coordinates. The general performance was demonstrated for an ideal tube. The high fiber stress gradients without residual stresses vanish to nearly constant fiber stresses over the wall-thickness after consideration of the residual stresses. In a second example it was shown that the method also works for patient-specific arteries obtained from medical imaging and allows to compute an estimate of the opened configuration. Finally we showed that the computed configurations are reasonable and therefore the residual stress estimation seems to be plausible.

Acknowledgements The authors greatly appreciate Dominik Brands and Sarah Brinkhues for their scientific support. Further, we gratefully acknowledge the financial support by the Deutsche Forschungsgemeinschaft (DFG) under the research grant SCHR 570/16-1.

References

V. Alastrué, E. Peña, M.A. Martínez, and M. Doblaré. Assessing the use of the "opening angle method" to enforce residual stresses in patient-specific arteries. *Annals of Biomedical Engineering*, 35:1821–1837, 2007.

R.P. Araujo and D.L. McElwain. The nature of the stresses induced during tissue growth. *Applied Mathematics Letters*, 18:1081–1088, 2005.

F. Auricchio, M. Conti, A. Ferrara, S. Morganti, and A. Reali. Patient-specific finite element analysis of carotid artery stenting: a focus on vessel modeling. *International Journal for Numerical Methods in Biomedical Engineering*, 29:645–664, 2013.

S. Avril, P. Badel, and A. Duprey. Anisotropic and hyperelastic identification of in vitro human arteries from full-field optical measurements. *Journal of Biomechanics*, 43:2978–2985, 2010.

E.U. Azeloglu, M.B. Albro, V.A. Thimmappa, G.A. Ateshian, and K.D. Costa. Heterogeneous transmural proteoglycan distribution provides a mechanism for regulating residual stresses in the aorta. *American Journal of Physiology – Heart and Circulatory Physiology*, 294:H1197–H1205, 2008.

P. Badel, K. Genovese, and S. Avril. 3D residual stress field in arteries: Novel inverse method based on optical full-field measurements. *Strain*, 48:528–538, 2012.

J.M. Ball. Constitutive inequalities and existence theorems in nonlinear elastostatics. In R.J. Knops, editor, *Symposium on Non-Well Posed Problems and Logarithmic Convexity*, volume 316. Springer-Lecture Notes in Mathematics, 1977.

D. Balzani, P. Neff, J. Schröder, and G.A. Holzapfel. A polyconvex framework for soft biological tissues. Adjustment to experimental data. *International Journal of Solids and Structures*, 43:6052–6070, 2006.

D. Balzani, J. Schröder, and D. Gross. Numerical simulation of residual stresses in arterial walls. *Computational Materials Science*, 39:117–123, 2007.

D. Balzani, D. Böse, D. Brands, R. Erbel, A. Klawonn, O. Rheinbach, and J. Schröder. Parallel simulation of patient-specific atherosclerotic arteries for the enhancement of intravascular ultrasound diagnostics. *Engineering Computations*, 29:888–906, 2012a.

D. Balzani, S. Brinkhues, and G.A. Holzapfel. Constitutive framework for the modeling of damage in collagenous soft tissues with application to arterial walls. *Computer Methods in Applied Mechanics and Engineering*, 213–216:139–151, 2012b.

W.C. Blondel, J. Didelon, G. Maurice, J.-P. Carteaux, X. Wang, and J.-F. Stoltz. Investigation of 3-D mechanical properties of blood vessels using a new in vitro tests system: Results on sheep common carotid arteries. *Transactions on Biomedical Engineering*, 48:442–451, 2001.

D. Brands, A. Klawonn, O. Rheinbach, and J. Schöder. Modelling and convergence in arterial wall simulations using a parallel FETI solution strategy. *Computer Methods in Biomechanics and Biomedical Engineering*, 11(5):569–583, 2008.

S. Brinkhues, A.-K. Tielke, and J. Schröder. Sensitivity analysis of plaque components within arterial wall simulations. *Proceedings in Applied Mathematics and Mechanics*, 10:73–74, 2010.

S. Brinkhues, A. Klawonn, O. Rheinbach, and J. Schröder. Augmented Lagrange methods for quasi-incompressible materials – Applications to soft biological tissue. *International Journal for Numerical Methods in Biomedical Engineering*, 29(3):332–350, 2013.

R. Bustamante and G.A. Holzapfel. Methods to compute 3D residual stress distributions in hyperelastic tubes with application to arterial walls. *International Journal of Engineering Science*, 48:1066–1082, 2010.

L. Cardamone, A. Valentin, J.F. Eberth, and J.D. Humphrey. Origin of axial prestretch and residual stress in arteries. *Biomechanics and Modeling in Mechanobiology*, 8:431–446, 2009.

Y.-C. Chen and J.F. Eberth. Constitutive function, residual stress, and state of uniform stress in arteries. *Journal of the Mechanics and Physics of Solids*, 60:1145–1157, 2012.

G.C. Cheng, H.M. Loree, R.D. Kamm, M.C. Fishbein, and R.T. Lee. Distribution of circumferential stress in ruptured and stable atherosclerotic lesions. A structural analysis with histopathological correlation. *Circulation*, 87:1179–1187, 1993.

C.J. Chuong and Y.C. Fung. On residual stress in arteries. *Journal of Biomechanical Engineering*, 108:189–191, 1986.

Y.C. Fung. What are the residual stresses doing in our blood vessels? *Annals of Biomedical Engineering*, 19:237–249, 1991.

Y.C. Fung and S.Q. Liu. Change of residual strains in arteries due to hypertrophy caused by aortic constriction. *Circulation Research*, 65:1340–1349, 1989.

Y.C. Fung and S.Q. Liu. Strain distribution in small blood vessels with zero-stress state taken into consideration. *American Journal of Physiology – Heart and Circulatory Physiology*, 262:H544–H552, 1992.

M.W. Gee, C. Förster, and W.A. Wall. A computational strategy for prestressing patient-specific biomechanical problems under finite deformation. *International Journal for Numerical Methods in Biomedical Engineering*, 26:52–72, 2010.

K. Genovese. A video-optical system for time-resolved whole-body measurement on vascular segments. *Optics and Lasers in Engineering*, 47:995–1008, 2009.

R. Glowinski and P. Le Tallec. Finite element analysis in nonlinear incompressible elasticity. In J.T. Oden and G.F. Carey, editors, *Finite elements, Vol V: Special Problems in Solid Mechanics*. Prentice-Hall, Englewood Cliffs, NH, 1984.

R. Glowinski and P. Le Tallec. *Augmented Lagrangian methods for the solution of variational problems*. Springer, Berlin, 1988.

R. Glowinski and P. Le Tallec. *Augmented Lagrangian and operator-splitting methods in nonlinear mechanics*, volume 9 of *SIAM Studies in Applied Mathematics*. Society for Industrial and Applied Mathematics (SIAM), Philadelphia, PA, 1989.

S. Govindjee and P.A. Mihalic. Computational methods for inverse finite elastostatics. *Computer Methods in Applied Mechanics and Engineering*, 136:47–57, 1996.

S. Govindjee and P.A. Mihalic. Computational methods for inverse deformations in quasi-incompressible finite elasticity. *International Journal for Numerical Methods in Engineering*, 43:821–838, 1998.

S.E. Greenwald, J.E. Moore, A. Rachev, T.P. Kane, and J.-J. Meister. Experimental investigation of the distribution of residual strains in the artery wall. *Journal of Biomechanical Engineering*, 119:438–444, 1997.

H.C. Han and Y.C. Fung. Species dependence of the zero-stress state of aorta: Pig versus rat. *Journal of Biomechanical Engineering*, 113:446–451, 1991.

M.R. Hestenes. Multiplier and gradient methods. *Journal of Optimization Theory and Applications*, 4:303–320, 1969.

G.A. Holzapfel and T.C. Gasser. Computational stress-deformation analysis of arterial walls including high-pressure response. *International Journal of Cardiology*, 116:78–85, 2007.

G.A. Holzapfel and R.W. Ogden. Modelling the layer-specific three-dimensional residual stresses in arteries, with an application to the human aorta. *Journal of the Royal Society Interface*, 7:787–799, 2010.

G.A. Holzapfel, T.C. Gasser, and R.W. Ogden. A new constitutive framework for arterial wall mechanics and a comparative study of material models. *Journal of Elasticity*, 61: 1–48, 2000.

G.A Holzapfel, G. Sommer, C.T. Gasser, and P. Regitnig. Determination of layer-specific mechanical properties of human coronary arteries with nonatherosclerotic intimal thickening and related constitutive modeling. *American Journal of Physiology – Heart and Circulatory Physiology*, 289:H2048–H2058, 2005.

G.A. Holzapfel, G. Sommer, M. Auer, P. Regitnig, and R.W. Ogden. Layer-specific 3D residual deformations of human aortas with non-atherosclerotic intimal thickening. *Annals of Biomedical Engineering*, 35:530–545, 2007.

G.A. Holzapfel, J.J. Mulvihill, E.M. Cunnane, and M.T. Walsh. Computational approaches for analyzing the mechanics of atherosclerotic plaques: a review. *Journal of Biomechanics*, 47:859–869, 2014.

W. Huang and R.T. Yen. Zero-stress states of human pulmonary arteries and veins. *Journal of Applied Physiology*, 85:867–873, 1998.

J. Kim and S. Baek. Circumferential variations of mechanical behavior of the porcine thoracic aorta during the inflation test. *Journal of Biomechanics*, 44:1941–1947, 2011.

Y. Lanir. Mechanisms of residual stress in soft tissues. *Journal of Biomechanical Engineering*, 31:044506–1 – 044506–5, 2009.

Z.-Y. Li, S. Howarth, R.A. Trivedi, J.M. U-King-Im, M.J. Graves, A. Brown, L. Wang, and J.H. Gillard. Stress analysis of carotid plaque rupture based on in vivo high resolution MRI. *Journal of Biomechanics*, 39:2611–2622, 2006.

J. Liu, X. Zhou, and M.L. Raghavan. Computational method of inverse elastostatics for anisotropic hyperelastic solids. *International Journal for Numerical Methods in Engineering*, 69:1239–1261, 2007.

S.Q. Liu and Y.C. Fung. Relationship between hypertension, hypertrophy, and opening angle of zero-stress state of arteries following aortic constriction. *Journal of Biomechanical Engineering*, 111:325–335, 1989.

H.M. Loree, A.J. Grodzinsky, S.Y. Park, L.J. Gibson, and R.T. Lee. Static circumferential tangential modulus of human atherosclerotic tissue. *Journal of Biomechanics*, 27:195–204, 1994a.

H.M. Loree, B.J. Tobias, L.J. Gibson, R.D. Kamm, D.M. Small, and R.T. Lee. Mechanical properties of model atherosclerotic lesion lipid pools. *Arteriosclerosis, Thrombosis, and Vascular Biology*, 14:230–234, 1994b.

J.F. Mulhern, T.G. Rogers, and A.J.M. Spencer. A continuum model for fibre-reinforced plastic materials. *Proceedings of the Royal Society London A*, 301:473–492, 1967.

J.C. Nagtegaal, D.M. Parks, and J.R. Rice. On numerically accurate finite element solutions in the fully plastic range. *Computer Methods in Applied Mechanics and Engineering*, 4:153–177, 1974.

J. Ohayon, O. Dubreuil, P. Tracqui, S. Le Floc'h, G. Rioufol, L. Chalabreysse, F. Thivolet, R.I. Pettigrew, and G. Finet. Influence of residual stress/strain on the biomechanical stability of vulnerable coronary plaques: Potential impact for evaluating the risk of plaque rupture. *American Journal of Physiology – Heart and Circulatory Physiology*, 293:H1987–H1996, 2007.

E. Peña, M.A. Martinez, B. Calvo, and M. Doblaré. On the numerical treatment of initial strains in biological soft tissues. *International Journal for Numerical Methods in Engineering*, 68:836–860, 2006.

S. Polzer, J. Bursa, T.C. Gasser, R. Staffa, and R. Vlachovsky. A numerical implementation to predict residual strains from the homogeneous stress hypothesis with application to abdominal aortic aneurysms. *Annals of Biomedical Engineering*, 41:1516–1527, 2013.

M.J.D. Powell. A method for nonlinear constraints in minimization problems. In R. Fletcher, editor, *Optimization*, pages 283–298. Academic Press, New York, 1969.

E.K. Rodriguez, A. Hoger, and A.D. McCulloch. Stress-dependent finite growth in soft elastic tissues. *Journal of Biomechanics*, 27:455–467, 1994.

N.V. Salunke, L.D.T. Topoleski, J.D. Humphrey, and W.J Mergner. Compressive stress-relaxation of human atherosclerotic plaque. *Journal of Biomedical Material Research*, 55:236–241, 2001.

J. Schröder. Anisotropic polyconvex energies. In J. Schröder and P. Neff, editors, *Poly-, Quasi- and Rank-One Convexity in Applied Mechanics, CISM Courses and Lectures*, volume 516, pages 53–105. Springer, 2010.

J. Schröder and S. Brinkhues. A novel scheme for the computation of residual stresses in arterial walls. *Archive of Applied Mechanics*, 84:881–898, 2014.

J. Schröder and P. Neff. Invariant formulation of hyperelastic transverse isotropy based on polyconvex free energy functions. *International Journal of Solids and Structures*, 40:401–445, 2003.

J. Schröder, P. Neff, and D. Balzani. A variational approach for materially stable anisotropic hyperelasticity. *International Journal of Solids and Structures*, 42:4352–4371, 2005.

M. Shams, M. Destrade, and R.W. Ogden. Initial stresses in elastic solids: Constitutive laws and acoustoelasticity. *Wave Motion*, 48:552–567, 2011.

J.C. Simo and R.L. Taylor. Quasi-incompressible finite elasticity in principal stretches. Continuum basis and numerical algorithms. *Computer Methods in Applied Mechanics and Engineering*, 85:273–310, 1991.

R. Skalak, S. Zargaryan, R.K. Jain, P.A. Netti, and A. Hoger. Compatibility and the genesis of residual stress by volumetric growth. *Journal of Mathematical Biology*, 34: 889–914, 1996.

A.J.M. Spencer. *Deformations of fibre-reinforced materials*. Oxford University Press, 1972.

L.A. Taber and J.D. Humphrey. Stress-modulated growth, residual stress, and vascular heterogeneity. *Journal of Biomechanical Engineering*, 123:528–535, 2001.

K. Takamizawa and K. Hayashi. Strain energy density function and uniform strain hypothesis for arterial mechanics. *Journal of Biomechanics*, 20:7–17, 1987.

M.T. Walsh, E.M. Cunnane, J.J. Mulvihill, A.C. Akyildiz, F.J.H. Gijsen, and G.A. Holzapfel. Uniaxial tensile testing approaches for characterisation of atherosclerotic plaques. *Journal of Biomechanics*, 47:793–804, 2014.

H.M. Wang, X.Y. Luo, H. Gao, R.W. Ogden, B.E. Griffith, C. Berry, and T.J. Wang. A modified Holzapfel-Ogden law for a residually stressed finite strain model of the human left ventricle in diastole. *Biomechanics and Modeling in Mechanobiology*, 13:99–113, 2014.

P.J. Zeller and T.C. Skalak. Contribution of individual structural components in determining the zero-stress state in small arteries. *Journal of Vascular Research*, 35:8–17, 1998.

X. Zheng and J. Ren. Effects of the three-dimensional residual stresses on the mechanical properties of arterial walls. *Journal of Theoretical Biology*, 393:118–126, 2016.